

High resolution sampling of methane transport in the Columbia River near-field plume: Implications for sources and sinks in a river-dominated estuary

A. S. Pfeiffer-Herbert,^{†*} F. G. Prahl, B. Hales, J. A. Lerczak, S. D. Pierce, M. D. Levine

¹College of Earth, Ocean, and Atmospheric Sciences, Oregon State University, Corvallis, Oregon

Abstract

Examining fluxes of biogeochemical constituents at the mouth of an estuary is necessary for assessing the modification of terrigenous-source materials in the estuary prior to reaching the ocean. In many rivers and estuaries, including the Columbia River estuary (CRE), methane is highly enriched with respect to oceanic concentrations and the equilibrium solubility of the atmospheric gas. We developed a methane budget for the CRE to examine the potential for significant modification of the estuarine methane budget by lateral exchange with peripheral tide flats. We accomplished the challenging task of constraining the net transfer through the estuary-ocean interface using novel instrumentation: a rapid methane analyzer combined with a membrane-contactor interfaced with a pumped-sampling undulating towed vehicle. Transport of riverine methane into the CRE was essentially balanced by losses due to flux to the atmosphere (42%), microbial oxidation in the water column (21%), and transport to the ocean (32%), suggesting limited net effect of lateral tide flat processes on the CRE methane budget. Estimated uncertainty bounds constrained lateral sink/source terms within -30% to $+20\%$ of the primary river input. This result contrasts with a number of prior studies of methane cycling in estuaries that reported dominant contributions from lateral sources and relatively minor export to the coastal ocean. The magnitude of lateral supply of methane is a useful indicator of the hydrologic source potential of other related signals of organic matter remineralization from anoxic or suboxic settings in the estuary.

Dissolved methane in coastal margin waters is characterized by strong river-to-ocean gradients. River concentrations are commonly supersaturated, with concentrations (of 10^1 – 10^3 nmol L^{-1}) that are one to three orders of magnitude greater than the solubility equilibrium with the partial pressure of methane in the atmosphere (2 – 3 nmol L^{-1}) (De Angelis and Lilley 1987; Sansone et al. 1999; Upstill-Goddard et al. 2000). Ocean concentrations, although still supersaturated in much of the surface ocean, are typically 5 nmol L^{-1} or less (Reeburgh 2007). Emission of methane from rivers and estuaries is estimated to be a minor component of the global atmospheric methane budget due to the small total area of these systems (Bange et al. 1994; Middelburg et al. 2002; Deborde et al. 2010), although the cycling and fate of methane between the river and ocean has only been examined for a limited range of estuary types (Borges and Abril 2012). Because processes affecting the hydrological supply of

methane from subsurface sediments also govern the supply of other products of organic matter remineralization generated in such settings by a range of suboxic and anaerobic microbial metabolisms (e.g., Deborde et al. 2008, 2010), improved understanding of methane dynamics at the land-to-sea margin benefits our knowledge of ecosystem-scale river and estuarine biogeochemical cycles.

Dissolved methane in rivers and estuaries can be viewed as a signature of hydrological input of anaerobic metabolic products occurring somewhere along the aquatic land-to-sea interface. Methanogenesis occurs in anoxic wetland soils (Le Mer and Roger 2001; Magonigal and Neubauer 2009) and submerged sediments (Kelley et al. 1995; Deborde et al. 2010) where sulfate is absent, either due to its complete consumption from seawater during anaerobic diagenesis or its naturally low concentration in fresh and brackish waters. Groundwater discharge is another highly concentrated methane source (Bugna et al. 1996; Jones and Mulholland 1998). Although methane production rates in these settings are very high, consumption by methanotrophs in the oxygenated surface layer of sediments efficiently reduces methane

[†]Present address: School of Natural Sciences and Mathematics, Stockton University, Galloway, New Jersey

*Correspondence: Anna.Pfeiffer-Herbert@stockton.edu

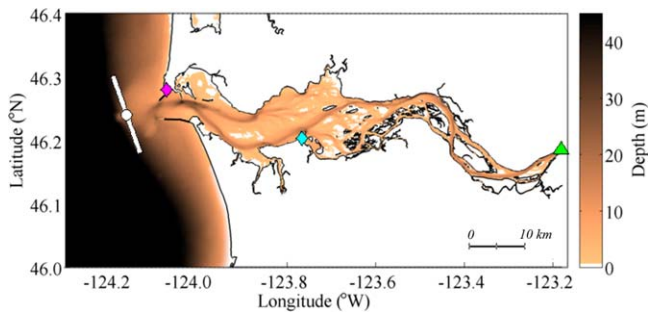


Fig. 1. Bathymetric map of the Columbia River estuary. White line is the survey track crossing the river plume, with circle marking the center reference point. Diamond markers show location of North Jetty tide station (magenta) and meteorological station at Astoria, Oregon (cyan). Green triangle is the USGS Beaver Army Terminal river gauge, the up-river boundary of the methane budget control volume.

emission to the overlying water (Kelley et al. 1995; Le Mer and Roger 2001; Deborde et al. 2010). Once in the water column, methane may be converted to carbon dioxide via oxidation by methanotrophs (De Angelis and Scranton 1993; Hanson and Hanson 1996) or lost to the atmosphere due to strong supersaturation of the dissolved methane and its fast exchange across the air–sea interface (De Angelis and Lilley 1987; Middelburg et al. 2002; Borges and Abril 2012). The balance of these sources and sinks will determine methane concentrations in estuarine waters and the subsequent partitioning of export between the atmosphere and coastal ocean.

Two major gaps remain in our understanding of estuarine methane budgets: (1) direct observations of estuary–ocean methane exchange and (2) importance of lateral supply of methane in river-dominated estuaries. Most previous methane budgets for estuaries were constructed from analysis of discrete water samples collected at relatively low temporal resolution along river and estuary channels (e.g., De Angelis and Scranton 1993; Zhang et al. 2008; Bussmann 2013). Stable isotopes have also been used to infer sources and sinks of methane in estuaries (Sansone et al. 1999; Bussmann 2013), as well as numerical models to track the fate of methane sources in the coastal ocean (Grunwald et al. 2009). Recently, instrumentation has been developed for continuous measurement of dissolved methane concentrations by laser spectroscopy using a membrane contactor interface (Gonzalez-Valencia et al. 2014). We combined a similar contactor system with rapid profiling capability to collect high resolution cross-sections of methane concentrations at the estuary–ocean boundary of the Columbia River.

The Columbia River estuary (CRE) has high methane inputs, with river-source water concentrations of 150–450 nmol L⁻¹ (Lilley et al. 1996), similar to other rivers globally (De Angelis and Lilley 1987; Middelburg et al. 2002; Bussmann 2013). The CRE is also rapidly flushed due to the large primary river discharge and tides (Neal 1972; Jay and

Smith 1990). Despite the river dominance, we have observed distinct spatial variability in methane within the CRE; specifically outflows from shallow lateral bays with methane concentrations at the end of ebb tides that are 2–8 times higher than the mainstem of the estuary at equivalent low salinities (F. Prahl, unpubl.). Elevated methane concentrations have also been noted at mid-estuary locations in other estuaries. Three European estuaries (Ems, Sado, and Scheldt) displayed methane concentration maxima at intermediate salinities that were coincident with the locations of drainage from tidal flats (Middelburg et al. 2002). Stable isotope signatures of methane in the Parker River estuary, Massachusetts and Great Bay, New Hampshire also indicated supply of methane at intermediate salinities, which was presumed to originate from salt marsh or sediment pore water (Sansone et al. 1999). In contrast to the Columbia, all of these estuaries have longer residence times and are dominated by marshy areas or other anoxic sediments, while the CRE has less than 25% shallow vegetated or tidal mud flat habitat by surface area (Simenstad et al. 1990). We constructed a methane budget for the CRE, using novel observations of transport through the estuary–ocean boundary combined with traditional data collection upstream, to address the question of whether lateral inputs of methane in the CRE significantly contribute to methane export from the system despite a large riverine source and rapid flushing of the estuary.

Methods

Study site

The Columbia River is the largest single freshwater source on the west coast of North America. Freshwater discharge ranges seasonally from 3000 to 12,000 m³ s⁻¹ with an annual mean of 5500 m³ s⁻¹ (Sherwood and Creager 1990; Simenstad et al. 1990). The estuarine portion of this large river ranges from 20 km to 50 km long as defined by salt intrusion but tidal influence on water elevation extends upstream to the Bonneville Dam at 235 km from the estuary mouth (Jay and Smith 1990). Average water depth is 7 m, with narrow channels that are dredged to 20–30 m deep and flanked by shoals (Fig. 1). Tides are mixed semidiurnal with amplitudes of 1–2 m in height and current speeds up to 3 m s⁻¹ near the CRE mouth. Estuary residence times are estimated to be 1–5 d over a range of river discharge and tides (Neal 1972; Jay and Smith 1990).

Methane budget

The primary goal of this study was to develop a methane budget for the lower Columbia River and assess the importance of internal methane sinks and sources relative to the primary river input. The control volume for the budget includes the freshwater tidal river downstream of Beaver Army Terminal (BAT) and brackish waters within ~40 km of the estuary mouth (Fig. 1). Transects of the near-field plume were used to represent the estuary–ocean boundary of the

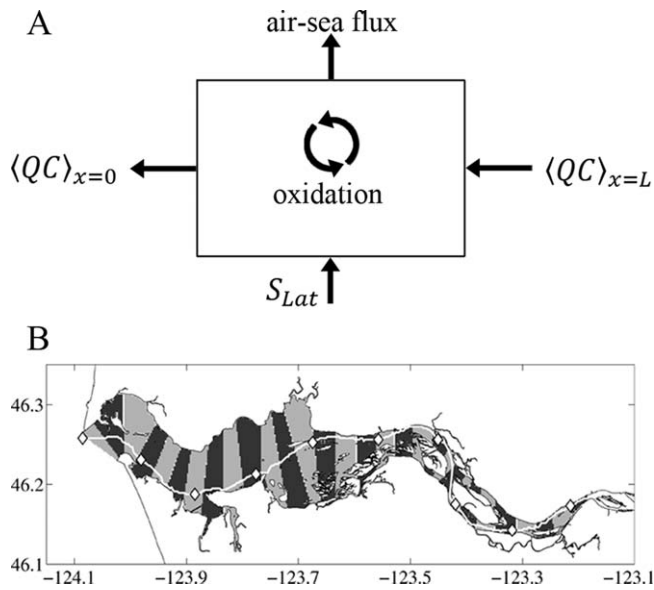


Fig. 2. (A) Schematic of methane budget for the lower Columbia River. Changes in methane in the control volume occur via transport of methane through the river ($\langle QC \rangle_{x=L}$) and ocean ($\langle QC \rangle_{x=0}$) boundaries, flux through the air-sea boundary, oxidation in the water column, and lateral sources (S_{Lat}). (B) Discretization of the control volume for methane loss model (Eqs. 7, 8) shown as shaded boxes. White diamonds indicate 10 km increments along the main channel of the estuary.

control volume, as described below (see “Plume transects”). The total pool of methane within the control volume, which we assume to be in steady state over a time scale of several days, depends on inward transport in at BAT, transport across the estuary-ocean boundary, loss due to air-sea gas exchange and microbial oxidation in the water column throughout the control volume, and residual source/sink terms required to close the budget (Fig. 2). We take these residual terms to represent the lateral supply (e.g., from anoxic settings within or bordering the estuary). We next describe the methods of estimating methane transport at the river and ocean boundaries, followed by the change in methane concentration due to air-sea exchange and aerobic microbial oxidation (“Methane loss model”).

Transport at river boundary

Transport of methane at the upstream river end of the control volume was based on discharge gauged at BAT multiplied by riverine methane concentration observed at the same location. Methane concentrations were measured in triplicate from water samples collected at three depths at BAT on 04 August 2010 by a headspace method described elsewhere (Anthony et al. 2012). The mean of these samples was multiplied by river discharge to obtain transport into the control volume at BAT ($\langle QC \rangle_{x=L}$ in Fig. 2). This calculation assumes that methane transport through the river boundary is dominated by advection of freshwater, which is a reason-

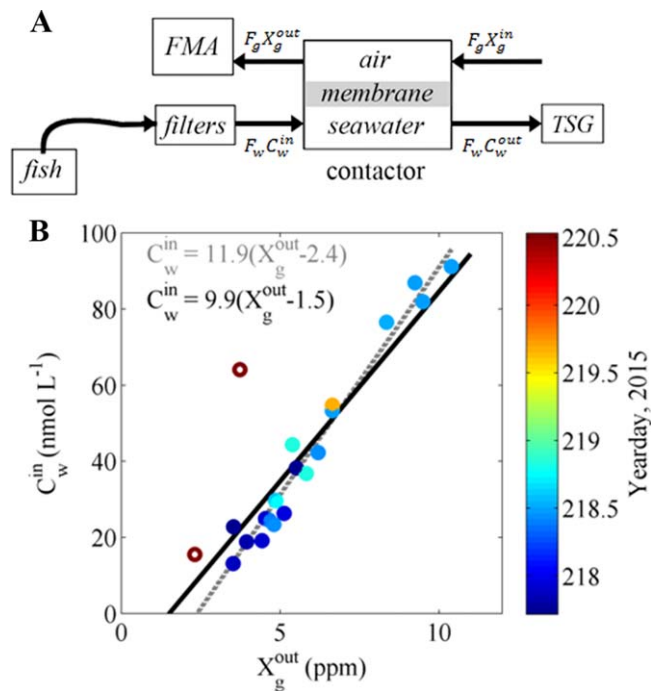


Fig. 3. (A) Schematic of flow-through system from SuperSucker fish through shipboard lab instruments. Filtered seawater and ambient air streams (with methane concentrations C_w^{in} and C_g^{in} , respectively) were pumped in opposing directions through the membrane contactor (at flow rates F_w and F_g , respectively). The carrier air was subsequently pumped to a fast methane analyzer (FMA) for analysis of methane concentration and the seawater stream passed through a thermosalinograph (TSG) for determination of time delay from the fish. (B) Calibration curve for methane detected by FMA/flow-through system (X_g^{out}) vs. measured by gas chromatography on gaseous headspace extracted from discrete water samples (C_w^{in}). Circles are calibration data points colored by time of sampling, dashed gray line is a linear regression of these data. Solid black line is a linear fit with a theoretical minimum X_g^{out} of 1.5 ppm (Eq. 1). Open circles are the last two samples collected during the survey, which were not included in the linear regressions.

able assumption due to the lack of density stratification to drive horizontal dispersion.

High-resolution methane measurements

Determining methane transports through the ocean boundary ($\langle QC \rangle_{x=0}$ in Fig. 2) involved novel use of instrumentation, which we describe in brief here. Methane data were collected with the “SuperSucker,” a towed vehicle (Hales et al. 2005, 2006; Holser et al. 2011) that is a winch-controlled modification of the Pumping SeaSoar (Hales and Takahashi 2002, 2004, 2012). A key innovation of these instruments is a pump integrated into the towed package to bring water onboard the ship for chemical analysis at rates approaching that at which the in situ hydrographic data are collected (Fig. 3A).

Seawater was pumped through a $\geq 50 \mu\text{m}$ filter and then through the shell-side of a microporous-membrane contactor (Liqui-Cel 2.5 \times 8, model G420, www.liquicel.com) at $\sim 6 \text{ L}$

min^{-1} (F_w , Fig. 3A). Room air was pumped in a counter direction through the contactor lumen-side at a precisely controlled 0.3 L min^{-1} (F_g). A mean mole fraction of 1.9 ± 0.1 ppm methane in the incoming room air (X_g^{in}) was observed in periodic measurements. The carrier gas has a methane signal imparted on it based on gas exchange through the hydrophobic membrane. The outlet composition is determined by a mass-balance controlled by that gas exchange and the ratios of the carrier-gas and seawater-sample streams. A mass-balance analysis was performed following the method of Bandstra et al. (2006) using discrete calibration samples collected from the seawater line and analyzed independently by a headspace method (Anthony et al. 2012). This analysis showed that the membrane contactor system was neither functioning at near-perfect equilibration as in the Hales et al. (2004) application of this system for pCO_2 , nor at highly efficient sparging as in the Bandstra et al. (2006) application for total dissolved CO_2 , but rather had a stripping efficiency of $\sim 25\%$ at the selected flow rates of F_w and F_g .

Whether viewed from the perspective of stripping efficiency (Bandstra et al. 2006), or the equivalent mass-transfer coefficient approach of Gonzalez-Valencia et al. (2014), the dissolved methane inlet concentration C_w^{in} (nmol L^{-1}) can be approximated by a linear model:

$$C_w^{\text{in}} = a(X_g^{\text{out}} - b) \quad (1)$$

where X_g^{out} is the analysis of the gas-stream mixing ratio (ppm) by a fast methane analyzer (FMA), and the coefficients a and b derive from the calibration samples. Based on the contactor efficiency or mass-transfer perspectives and the calibration samples, we found that the value of b , corresponding to the minimum-allowable value of X_g^{out} for the hypothetical situation where $C_w^{\text{in}} = 0$, was 1.5 ppm. A slope fitted to the calibration samples from a fixed intercept of b yielded a value of 9.9 for a in Eq. 1 (black line in Fig. 3B). The selected calibration curve fell within the 95% confidence interval of a least-squares regression of the calibration samples (gray line in Fig. 3B) and avoided prediction of negative C_w^{in} in the lowest concentration samples.

This relationship was robust for all calibration samples analyzed up through day 220 (Fig. 3B). Two calibration samples collected at day 220.5 yielded significantly lower mass-transfer coefficients, or contactor efficiencies, and fell off this calibration relationship. We do not know if the lower efficiencies indicate a systematic decline in the performance of the contactor membrane from the closest previous calibration point (on day 219.7) through the end of the survey. Noting the greater uncertainty about the contactor efficiency in the final three transects, we assumed that Eq. 1 calibration was reasonably constant throughout the 3 d sampling period described below (“Plume survey”).

Synchronization of chemical and physical measurements

Mapping methane concentrations to vertical profiles of the SuperSucker required careful matching of salinity on the towed fish with salinity measured at the shipboard lab (Fig. 3A) and attention to additional instrument time lags. Delays of 4.7–5.1 min between the SuperSucker fish and the pumped samples arriving in the lab were estimated by fitting a lag plus offset between salinity measured at the fish and salinity measured by a thermosalinograph in the lab in a 300 s time window at increments of 150 s. This procedure for estimating time delays has been demonstrated to have errors < 5 s (Hales and Takahashi 2002). An additional lag of 27 ± 4 s between the thermosalinograph and the methane analyzer was estimated by lagged cross-correlation between methane and salinity, assuming an inverse linear relationship between methane and salinity. The analysis of thermosalinograph-methane analyzer lag was constrained within a 20 min time window advanced in 5 min increments along the time series. Methane data were corrected for these time lags to align with in situ measurements.

Water transport

Velocity profiles were collected with two Teledyne RD Instruments Workhorse broadband acoustic Doppler current profilers (ADCP). A 600 kHz ADCP was boom-mounted at a depth of 1 m, with the shallowest available data at 2 m. These data were collected in 0.5 m vertical depth bins and processed with 1 min ensemble averaging. Inherent random ADCP velocity uncertainty for a 1 min ensemble was estimated to be 0.02 m s^{-1} . Because the boom-mounted 600 kHz ADCP data were poor quality below ~ 25 m, these data were supplemented with a hull-mounted 300 kHz ADCP in deeper locations. The 300 kHz data were collected in 4 m vertical bins and processed with 2 min ensemble averaging. The shallowest available data from the 300 kHz instrument was at 13 m. The two ADCP records were merged by a linearly weighted average between the shallowest available 300 kHz measurement (usually 13 m) and the deepest available 600 kHz measurement. Due to side lobe interference (RDI 2011), gaps of 3–15 m remained at the bottom.

Plume survey

Navigational constraints prevented towing the SuperSucker within the confines of the Columbia River mouth. Instead, repeated transects crossing the Columbia River plume at approximately 6 km away from the estuary mouth were conducted on 05–08 August 2010 (Fig. 1). The survey spanned six semidiurnal tide cycles with some gaps due to unexpected instrument malfunction and repairs (Fig. 4). Individual transects covered distances of at least 13 km and were transited (at ship speeds of ~ 2 kts) in 3.2–3.9 h. SuperSucker profiles covered depths of 0.5 m below the surface to 2 m above the sea floor, with vertical profiling rates of $10\text{--}20 \text{ cm s}^{-1}$. Vertical profiles of the ~ 40 m water column were thus completed in 4–8 min such that each transect consisted

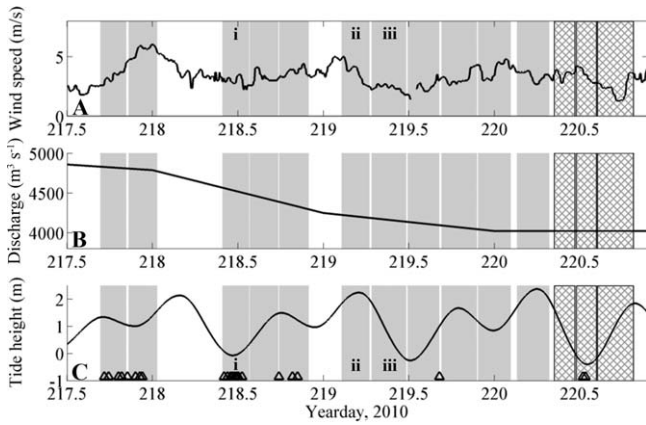


Fig. 4. Environmental conditions during the SuperSucker survey. **(A)** Wind speed at Astoria, Oregon. **(B)** Columbia River daily average discharge at Beaver Army Terminal. **(C)** Tide height at North Jetty, the mouth of the estuary. Timing of individual transects are denoted by shaded bars (solid: full line covered, cross-hatch: partial coverage) and white bars are data gaps or periods when the ship was turning. Triangles indicate times when methane calibration samples were collected. Roman numerals mark sample transects during (i) major ebb (Fig. 6A), (ii) major flood (Figs. 5A–C, 6C), and (iii) major ebb (Figs. 5D–F, 6B).

of a few dozen profiles with nominal horizontal separation of ~ 200 – 400 m. Vertical resolution of the various measurements corresponded to the response-time of each measurement multiplied by the vertical profiling rate (i.e., ~ 1.5 m for methane).

Calculating plume transports

Data from the ADCP and SuperSucker were projected onto a common straight transect line (Fig. 1) with distance along the line calculated in kilometers from a reference point centered on the Columbia River mouth (46.240°N , 124.162°W). SuperSucker data were mapped onto a uniform grid of 50 m horizontally and 0.2 m vertically by inverse square reduced distance-weighted averaging, as in Hales et al. (2006). Reduced distances were normalized by 0.2 m in the vertical and 0.2 km in the horizontal, and only points within 10 reduced distances were included in the average for each grid point.

SuperSucker and ADCP data were extrapolated to the sea surface by assuming a uniform value from the shallowest measurement to the surface. The shallowest data points prior to extrapolation were at 2 m in the case of ADCP velocity data and 0.5–1 m for SuperSucker data. As stated above, the ADCP data typically missed 3–15 m at the bottom (10–40% of the water column), with greater loss in deeper water. To assess the sensitivity of transport calculations to the missing velocity information near the seafloor, data were extrapolated to the bottom by assuming zero velocity at the seafloor and uniform near-bottom salinity and methane. In all other cases, the deep areas with missing velocity were omitted from transport calculations.

The gridded SuperSucker and ADCP data were used to estimate transport across the transect line. Net volume flow in $\text{m}^3 \text{s}^{-1}$ through each grid cell (j, k) was calculated as

$$Q_{\text{vol},jk} = -u_{jk}\Delta y\Delta z \quad (2)$$

where u_{jk} is transect-normal velocity (positive in the onshore direction) in m s^{-1} , Δy is horizontal bin width (50 m) and Δz is vertical bin height (0.5 m). Methane and freshwater transports through grid cells were calculated by

$$(QC)_{jk} = C_{jk}Q_{\text{vol},jk} \quad (3)$$

where C_{jk} is the concentration of the constituent of interest. Freshwater transport was determined by freshwater fraction, $C_{FW,jk} = \frac{S_0 - S_{jk}}{S_0}$, calculated from measured salinity (S_{jk}) relative to a reference salinity S_0 . An S_0 of 32.5 was selected to represent shallow coastal waters, the marine end-member of mixing in the plume (Barnes et al. 1972). Tidally averaged freshwater transport only decreases by 6% if S_0 is reduced to 32 (as in Hickey et al. 1998; Horner-Devine 2009) or increases by 6% if S_0 is increased to 33 (as in Nash et al. 2009).

Tidally averaged transports were calculated as an estimate of net transport in or out of the estuary. Because sampling intervals were not evenly distributed across the tide cycle, data were bin-averaged by fraction of the semidiurnal tide (τ^*), defined as $\tau^* = \frac{\tau_t - \tau_p}{\tau_N - \tau_p}$, where τ_t is the time of the data point, τ_p is the time of the previous slack water before ebb, and τ_N is the time of the next slack before ebb. Bin intervals of 0.2 (five bins total) were used for averaging by τ^* . Within a distance range of ± 5 km, 89% of the horizontal grid cells had full tide cycle coverage of both velocity and salinity data and all of the remaining grid cells had data in at least four of the five τ^* bins. Incomplete coverage over the tide cycle occurred at 2.3–2.7 km north of the transect center, which lacked observations during low tide ($0.2 < \tau^* < 0.4$), and 2.9–3.4 km north of the transect center, which lacked observations during high tide ($0.6 < \tau^* < 0.8$). Data at each grid cell were first averaged within τ^* bins to produce $(QC)_{jk,\tau^*}$ and then averaged across the τ^* bins as

$$\langle \bar{QC} \rangle_{jk} = \frac{1}{5} \sum_{\tau^*=1}^5 (QC)_{jk,\tau^*} \quad (4)$$

to produce a tidally averaged transport through the grid cells. Finally, total tidally averaged transports were calculated by integrating the results of Eq. 4 across the section:

$$\langle QC \rangle = \sum_{j=-5}^5 \sum_{k=0}^H \langle \bar{QC} \rangle_{jk} \quad (5)$$

$\langle QC \rangle$ in Eq. 5 is a direct estimate of the tidally averaged transport through the ocean boundary of the control volume, equivalent to $\langle QC \rangle_{x=0}$ in Fig. 2.

Assessment of temporal aliasing

Aliasing of the tide cycle could result from inadequate temporal coverage of the plume transects. To assess the effects of our sampling scheme on temporal aliasing of tidally averaged transports we employed output from a numerical model. The Semi-implicit Eulerian-Lagrangian Finite Element (SELFE) model is a finite-volume unstructured grid model that has reasonable skill in simulating the CRE hydrodynamics (Baptista et al. 2005; Zhang and Baptista 2008; Kärrnä et al. 2015). For the purposes of this study we did not attempt a direct model-data comparison, but rather subsampled the numerical model against itself to test the impact of nonuniformity in sampling on the resultant tidally averaged transports. The advantage of a numerical model is that its output is available continuously in time and space. Velocity and salinity fields were extracted from an August 2010 SELFE hindcast simulation at the location of the SuperSucker transects. Volume and freshwater transports were calculated from SELFE velocity and salinity with (1) 15-min time step at every grid point and (2) model output subsampled to match the SuperSucker transects.

Methane loss model

Conservation of methane in the control volume was defined as

$$A_{cs} \frac{\partial C}{\partial t} = \frac{\partial}{\partial x} \left[Q_R C + A_{cs} D_H \frac{\partial C}{\partial x} \right] + A_{cs} \left[\frac{e_g}{H} (C_{sat} - C) - \alpha_{ox} C + S_{Lat} \right] \quad (6)$$

where C is methane concentration (mol m^{-3}), A_{cs} is tidally averaged cross-sectional area, x is along-channel distance, Q_R is freshwater discharge at BAT ($\text{m}^3 \text{d}^{-1}$), D_H is horizontal eddy diffusivity ($\text{m}^2 \text{d}^{-1}$), e_g is gas transfer velocity (m d^{-1}), C_{sat} is the saturation concentration of methane, α_{ox} is a water column methane oxidation rate (d^{-1}), and S_{Lat} encompasses additional sources of methane ($\text{mol m}^{-3} \text{d}^{-1}$) between the river and estuary mouth. All of the above quantities are assumed to be averaged over sufficiently long periods to remove the influence of tides. On the right hand side, the first two terms are advection and dispersion of methane, respectively, and the last three terms are sources (S_{Lat} , presumed to derive from lateral input) and sinks (air-sea exchange and aerobic microbial consumption) of methane within the control volume.

We applied the following simplifying assumptions to Eq. 6. First, the system was in steady state ($\frac{\partial C}{\partial t} = 0$) over the week-long time frame of our study and laterally well-mixed. Second, along-channel dispersion is small enough to be neglected ($\frac{\partial Q_R C}{\partial x} \gg \frac{\partial}{\partial x} A_{cs} D_H \frac{\partial C}{\partial x}$). We estimated the along-channel dispersion of methane to be at least an order of magnitude smaller than the advection term based on a previous estimate of D_H in the CRE (MacCready 2011). Finally, we consider a null hypothesis that S_{Lat} is zero. The remaining terms were integrated along the control volume from $x = L$ (BAT) to $x = 0$ (estuary mouth) as the following approximation:

$$\langle QC \rangle_{x=L} - \langle QC \rangle_{x=0} = -A_{cs} \int_0^L \left[\frac{e_g}{H} (C_{sat} - C) - \alpha_{ox} C \right] dx \quad (7)$$

The right-hand side of Eq. 7 describes changes in methane transport between the river and ocean boundary due to losses by air-sea exchange and microbial oxidation. This integral was solved by discretization of the control volume into segments with widths of 3 km along the axis of the main channel (Fig. 2). An analytical solution for change in methane concentration over time was applied within each segment:

$$C_{\Delta t} = \frac{e_g}{H} C_{sat} \left(1 - e^{-\left(\frac{e_g}{H} + \alpha_{ox}\right) \Delta t} \right) + C_o e^{-\left(\frac{e_g}{H} + \alpha_{ox}\right) \Delta t} \quad (8)$$

The time scale Δt was defined by the volume of segment i divided by Q_R . Temperature and salinity, used to calculate e_g and α_{ox} , were obtained from a down-estuary transect on 04 August 2010 using the shipboard flow-through system with an intake depth of 5 m. An initial concentration of 300 nmol L^{-1} was applied to the segment at $x = L$ and the initial concentration of each subsequent segment ($C_{o,i}$) was determined by the final concentration of its upstream neighbor ($C_{\Delta t, i-1}$).

Segment volume was obtained from a combination of available high resolution bathymetry data sources. In the area of interest these data were the NGDC one third arc-second digital elevation model for Astoria, Oregon (Carignan et al. 2009), a bathymetry and LiDAR data product for the upper estuary from the Oregon Department of Geology and Mineral Industries (<http://www.oregongeology.org>), and a 2012 U.S. Army Corps of Engineers bathymetry survey of the lower estuary (<http://www.nwp.usace.army.mil/Missions/Navigation/surveys.aspx>).

The gas transfer coefficient in Eq. 8, e_g (m d^{-1}), was parameterized as a function of wind speed at 10 m height (u_{10} , m s^{-1}) as in Wanninkhof (2014):

$$e_g = \frac{1.55 \langle u_{10}^2 \rangle}{\sqrt{Sc}} \quad (9)$$

where $\langle u_{10}^2 \rangle$ is the mean of squared wind speeds and Sc is a temperature- and salinity-dependent Schmidt number for methane. Wind speeds were obtained from a meteorological tower in Astoria, Oregon (NOAA National Ocean Service station at 46.208°N , 123.767°W). A single value of $\langle u_{10}^2 \rangle$ was calculated from winds measured every 6 min on days 214–219 as a base case (partial wind time series appears in Fig. 4A). The 6-d time period was selected to represent the residence time in the control volume, as estimated from river discharge and total volume. We also calculated $\langle u_{10}^2 \rangle$ daily during that week and solved Eq. 8 with the minimum and maximum daily means to estimate temporal variability in methane flux to the atmosphere. A spatially varying Sc was

Table 1. CRE methane budget terms (in mol d⁻¹) and range of uncertainty. Sources of uncertainty that were not quantified are listed in italics.

Budget term	Baseline estimate	Uncertainty bounds	Source of uncertainty
River transport	11.5 × 10 ⁴	10.4 × 10 ⁴ 12.8 × 10 ⁴	Lowest daily averaged river discharge Highest daily averaged river discharge <i>Concentration vs. discharge</i> <i>Lateral variability in river methane</i>
Methane loss model	-7.2 × 10 ⁴	-6.0 × 10 ⁴ -8.1 × 10 ⁴	Lowest daily averaged wind speed, highest daily averaged river discharge Highest daily averaged wind speed, lowest daily averaged river discharge <i>Spatial variability in wind speed</i> <i>River methane variability</i> <i>Site-specific gas exchange and methane oxidation rates</i>
Plume transport	-3.7 × 10 ⁴	-3.1 × 10 ⁴ -4.3 × 10 ⁴ -5.0 × 10 ⁴	Temporal aliasing* Velocity shear at surface Lower seawater methane concentration [†]

*Numerical model result.

[†]12 nmol L⁻¹ instead of 19 nmol L⁻¹ applied to missing landward volume transport (see “Methane transport in plume”). 12 nmol L⁻¹ is the mean concentration observed in high salinity water deeper than 30 m.

calculated from shipboard flow-through temperature and salinity using the equation of Wanninkhof (2014).

Gas exchange also depends on the concentration gradient between the atmosphere and surface water. Our shipboard measurement of atmospheric methane in air was 1.9 ppm, comparable to the global atmospheric methane mole fraction in 2010 of approximately 1.8 ppm (WMO 2011). The shipboard observation provides C_{sat} of 2.8 nmol L⁻¹ based on solubility coefficients from Wiesenburg and Guinasso (1979) at the mean water temperature (19.6°C) and salinity (3.5) in the control volume.

Rates of methane oxidation, α_{ox} , were obtained from the literature. Separate α_{ox} values were selected for fresh and saline water based on ¹⁴C-CH₄ incubation experiments in the Hudson River that revealed a rapid decrease in oxidation rate in the salinity range of 3–7 (De Angelis and Scranton 1993). One observation of methane oxidation in the Columbia River in October 1988 suggested a specific methane oxidation rate of 0.05 d⁻¹ (Lilley et al. 1996). Methane oxidation rates vary with temperature in addition to salinity (Hanson and Hanson 1996; Reeburgh 2007). Adjusting for a 5°C climatological temperature difference between early August and October with a Q_{10} of two (De Angelis and Scranton 1993), we applied a specific methane oxidation rate of 0.08 d⁻¹ for salinity below 3. Reported oxidation rates in oceanic water are 5×10^{-5} to 5×10^{-2} d⁻¹ (Ward et al. 1987, 1989; De Angelis and Scranton 1993). We selected α_{ox} of 0.001 d⁻¹ for salinity greater than 7, and scaled the rate linearly with salinity between 3 and 7. The predicted loss of methane in the control volume was not sensitive to the

choice of α_{ox} for higher salinity within the range of reported oxidation rates.

Results

Methane transport in river

Transport of methane into the control volume through the river boundary was three times higher than the outward methane transport observed in the plume (Table 1). The river methane transport estimate was based on a single set of water samples collected on 04 August 2010 at one station, thus it is important to consider whether it is appropriate to extrapolate these data to the full cross section. We do not have any observations of cross-channel variability in methane at BAT, but a vertical profile was collected at the sampling location. The range of methane concentrations observed from surface to bottom was 298–306 nmol L⁻¹, within 2% of the mean.

A limited number of methane concentrations at BAT were also available from other years for comparison with our survey. The riverine methane concentration was similar to this study in September 2009 (320 nmol L⁻¹) but considerably lower in September 2008 (215 nmol L⁻¹). River discharge was ~3000 m³ s⁻¹ in both September sampling periods. Methane concentration at BAT in late April 2013 was 175 nmol L⁻¹; however, because river discharge was a factor of two higher the methane loading from the river then would have been similar to our study period. Another benchmark of methane variability comes from a 2-yr long time series of methane concentration in the Willamette River, a tributary of the Columbia River. Weekly variation in summertime

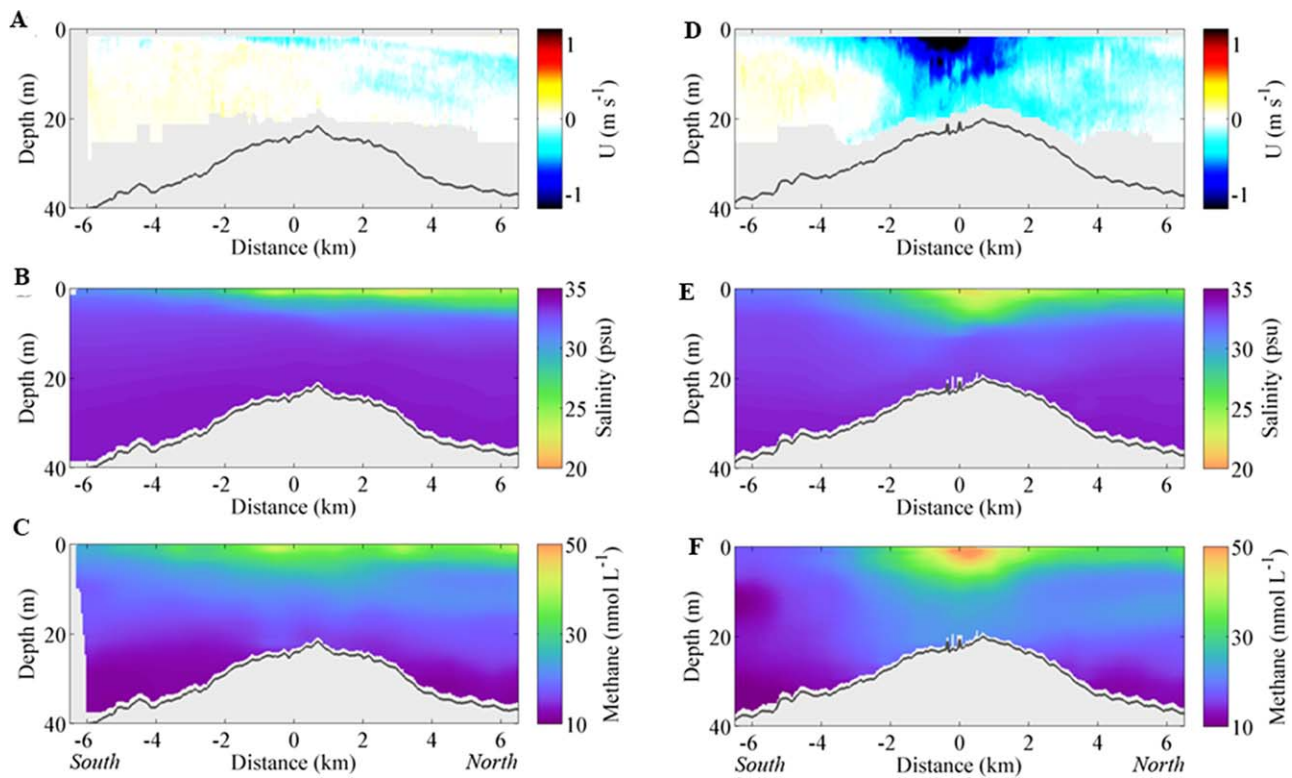


Fig. 5. Examples of plume sections collected during (A–C) a major flood tide on day 219.10–219.27 (transect *ii* in Fig. 4) and (D–F) a major ebb tide on day 219.28–219.48 (transect *iii* in Fig. 4). From top to bottom, panels show transect-normal velocity (positive toward shore), salinity, and methane concentration. Light gray shading is in areas with no data and dark gray line is the water depth.

methane concentration in the Willamette was typically within $\pm 25\%$ of the seasonal mean and spatial gradients were within $75 \text{ nmol L}^{-1} \text{ km}^{-1}$ along channel and $\sim 50 \text{ nmol L}^{-1}$ cross-channel (Anthony et al. 2012). Our assumption of uniform river methane input thus appears to be reasonable over the week-long residence time relevant to our survey.

Methane transport in plume

SuperSucker transects of the estuarine plume produced detailed cross-sections of velocity, salinity, and methane such as the examples in Fig. 5. Methane in plume cross-sections appeared as the inverse of salinity (Fig. 5). In the lowest salinity water observed (~ 10 psu), methane concentrations reached 100 nmol L^{-1} (Fig. 6A). Methane concentrations in the saltiest coastal waters were as low as 5 nmol L^{-1} but averaged 19 nmol L^{-1} in water with salinity greater than 32.5. For salinity less than 32.5, methane-salinity correlations within each transect had $R^2 = 0.49\text{--}0.79$. Linear fits between methane and salinity for two transects associated with major ebb tides extrapolate to $>100 \text{ nmol L}^{-1}$ at zero salinity (Fig. 6A,B). Other transects prior to day 220 had y -intercepts of $80 \pm 10 \text{ nmol L}^{-1}$ (e.g., Fig. 6C).

Transports of volume and concentration were integrated across individual sections to examine time variability. Section-integrated transports were calculated from Eqs. 2

and 3 across distances within 5 km of the center (where tidal cycle coverage was consistent across the majority of transects) and from the surface to bottom or deepest available depth. These transports were compared as a function of time relative to low tide at the North Jetty of the CRE entrance (Fig. 7). Volume transport was directed offshore between 6 h before low tide and 1.7 h after low tide with peak seaward transport within 3 h of low tide (Fig. 7A). Net shoreward volume transport was observed in sections collected between 1.7 h and 5.4 h after low tide. The cycle of volume transport compares favorably with prior observations of peak offshore discharge at 1 h before low tide and shoreward volume transport 2–6 h after low tide (Kilcher and Nash 2010). Maximum observed offshore transport was 4.6 times higher than maximum onshore transport, suggesting a strong ebb tide plume emerging from the estuary and weaker return on the flood tide as is visible in Fig. 5 (D–F vs. A–C, respectively).

Section-integrated transports of freshwater and methane were directed offshore over the full tide cycle (Fig. 7B,C). The maximum offshore transports of freshwater and methane appeared delayed relative to the observed peak in volume transport (Fig. 7), but the actual peak transports may have been missed due to lack of sampling 0–2 h before low tide. Minimum transports of both properties fell between 4 h and 6 h after low tide. The maximum observed volume transport

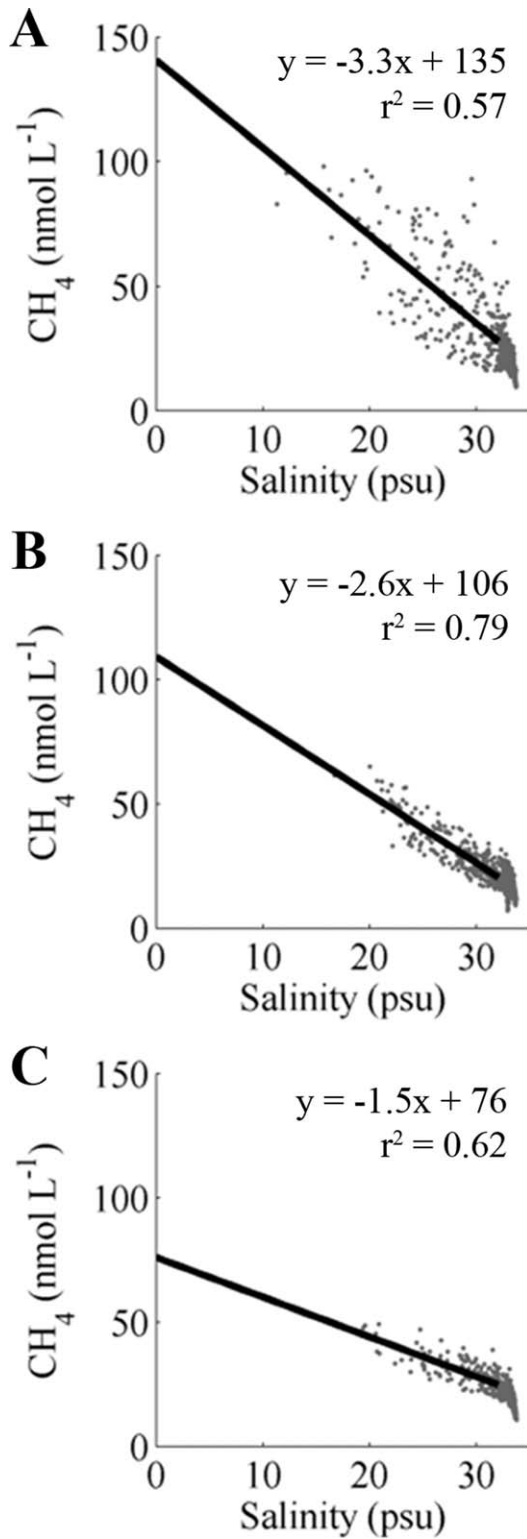


Fig. 6. Methane–salinity relationships in three sample transects, surveyed during (A) major ebb tide on day 218.5 (*i* in Fig. 4), (B) major ebb tide on day 219.4 (*iii* in Fig. 4), (C) major flood tide on day 219.2 (*ii* in Fig. 4). Gray dots are individual data points from each transect (subsamped for visual clarity) and black lines are the best linear fit to data points with salinity less than 32.5 psu, extrapolated to the freshwater intercept.

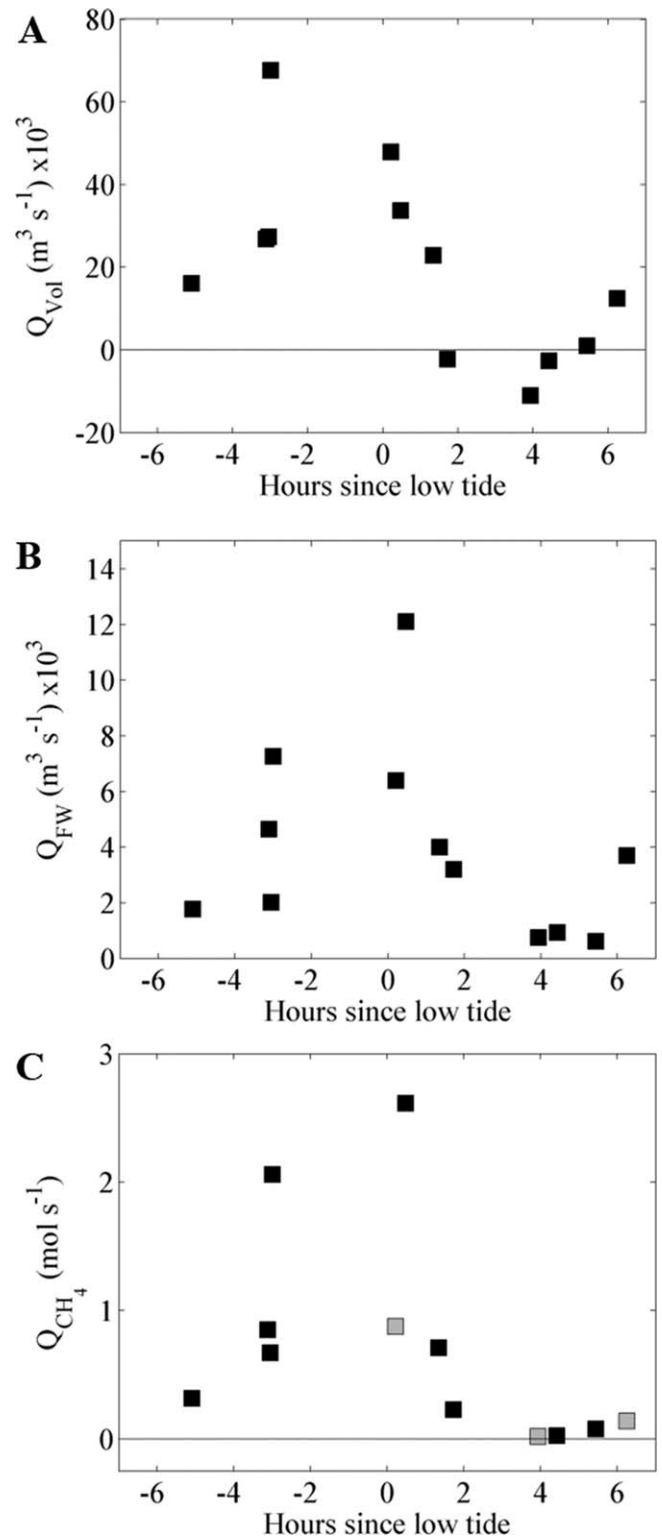


Fig. 7. Spatially integrated transports of (A) volume, (B) freshwater, and (C) methane per section plotted by time relative to low tide at the estuary mouth. Markers are placed at the time that the ship passed the transect center point, although the full duration of each transect was ~3 h. Gray markers indicate transects at end of survey with higher uncertainty in methane concentration.

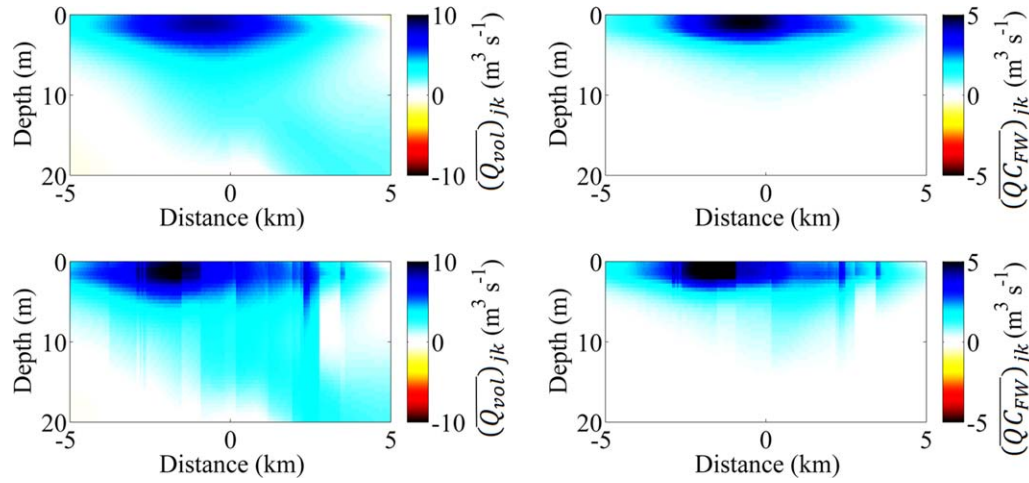


Fig. 8. Tidally averaged transport across transect line from numerical model output used to test effects of temporal aliasing in the sampling scheme. (A) Volume flux and (B) freshwater flux through each grid calculated from continuous 15-min model output. (C) Volume flux and (D) freshwater flux through each grid calculated from model output that was subsampled to match timing of observations.

was during an early major ebb tide, while the maximum observed freshwater and methane transports occurred at the end of a major ebb. Transects conducted near the end of the survey that may have been affected by downward drift in methane concentration (see “High resolution methane measurements”) are denoted with gray markers in Fig. 7. Despite relatively low methane concentrations, the integrated methane transports from these sections had a tidal cycle trend similar to the equivalent section-averaged freshwater transports. We retained the methane data from the end of the survey in the calculation of tidally averaged transport.

The purpose of conducting repeat transects across the CRE plume was to estimate tidally averaged transport of methane through the estuary-ocean boundary. Application of Eq. 5 to velocity, salinity, and methane transect data resulted in tidally averaged, section-integrated, transports listed in Table 1. There are three primary sources of uncertainty in these transport results: uneven coverage of the tide cycle, missing data near surface and bottom, and gaps between the transect line and coastline.

Potential aliasing error in tidally averaged transports due to irregular sampling over the tide cycle was estimated with numerical model output (see “Assessment of temporal aliasing”). Both the continuous and subsampled model output reproduced the pattern of strong offshore transport through the shallow central region of the transect line and weak onshore transport in portions of the deeper layer (Fig. 8). Total volume transport over the course of the survey period was 19% higher when calculated from the subsampled model output compared with the continuous model output. Similarly, total freshwater transport from subsampled model output was 14% higher than continuous output. The difference between the continuous time and subsampled transports in the model suggests that tidal aliasing in the

SuperSucker sampling scheme potentially overestimated the size of tidally averaged volume and freshwater transport, and methane transport by corollary, because of the strong inverse dependence of methane concentration on salinity.

The tidally averaged transports were sensitive to the method of extrapolating profile data to the surface but insensitive to extrapolation from the deepest measurements to the seafloor. Velocity data had a relatively large gap from the deepest recovered bin to the seafloor (up to 40% of the total water depth). Extrapolation from the shallowest measured velocities (2 m) to the surface impacts total transport because velocities in the near-field plume region are maximal near the surface (Orton and Jay 2005; Nash et al. 2009). As a conservative estimate of surface transport, we chose to extrapolate velocities as a uniform value from 2 m to the surface. This extrapolation increases the observed total volume transport by 35%. If we instead assumed constant shear to the surface, tidally averaged transports would be 15–20% larger than the uniform surface velocity method. In contrast, any reasonable approach to extrapolation of our deepest transport observations to the bottom made little difference in the transport estimates (<2% change in total volume transport).

The placement of SuperSucker transects offshore of the estuary mouth raised an additional complication of not having a fully enclosed boundary. Ocean-estuary exchange through gaps between the transect line and the shoreline was not measured. A complete cross-section within the estuary should have net volume transport equal to the freshwater transport if averaged over a sufficient number of tidal cycles. However, our estimated total through-section transport was a seaward flow that exceeded the river flow by a factor of five. A correction factor for tidally averaged methane transport was estimated to account for this difference.

First, we observed that the near-field plume sections appeared to capture the majority of the new estuarine outflow on the basis of isohaline outcropping and the freshwater budget. Prior studies identified the base of the ebb tide plume at salinities between 21 and 26 (Cudaback and Jay 2000; McCabe et al. 2008; Horner-Devine et al. 2009). In our survey the 22–24 psu isohalines, when present, outcropped to the surface in two places within 4 km of the transect center (e.g., Fig. 5E), indicating that the estuary outflow was fully captured on ebb tides. Furthermore, tidally averaged freshwater transport estimated from the plume transects was $4570 \text{ m}^3 \text{ s}^{-1}$, within the range of the daily-averaged gauged freshwater input to the estuary in the week of the survey ($4020\text{--}4930 \text{ m}^3 \text{ s}^{-1}$).

Second, since our estimate of freshwater outflow at the plume was in good agreement with the primary river input, we made an assumption that the missing landward flow was predominantly high salinity coastal ocean water that flowed beneath or around the sides of the transect line. The mean methane concentration in waters with salinity greater than 32.5 was 19 nmol L^{-1} . The amount of landward transport required for volume balance is $19 \times 10^3 \text{ m}^3 \text{ s}^{-1}$. Combining the coastal ocean methane concentration and volume transport residual suggested missing landward methane transport of 0.38 mol/s , reducing the directly observed net offshore methane transport (0.81 mol/s) by 50%. The corrected methane transport is reported in Table 1.

Integrated losses due to air–sea gas exchange and microbial oxidation

The methane loss model described by the right-hand side of Eq. 7 provided estimates of changes in methane concentration expected from air–sea gas exchange and oxidation by methanotrophs in the water column. This model predicted a loss of approximately two-thirds of the methane between the river and ocean boundaries of the control volume (Table 1; Fig. 9), decreasing the concentration from 300 nmol L^{-1} at BAT to 113 nmol L^{-1} at the estuary mouth under wind and river discharge averaged over a 6 d period at the time of the survey (Fig. 9). The rate of methane loss due to air–sea exchange was approximately twice as large as the loss due to methane oxidation.

The methane loss model results were less sensitive to river discharge than to variability in wind speed and initial methane concentration. Minimum and maximum daily river discharge within a week of the survey produced a $\pm 10\%$ change in methane concentration at the ocean boundary and $\pm 4\%$ change in total methane loss. Variability in daily mean squared wind speed altered methane concentration at the mouth by $\pm 33\%$ and total methane loss by $\pm 19\%$ compared with the base case of 6-d averaged winds. Based on weekly percent variability of methane concentrations in the nearby Willamette River (Anthony et al. 2012), the predicted methane loss might vary by as much as $\pm 25\%$.

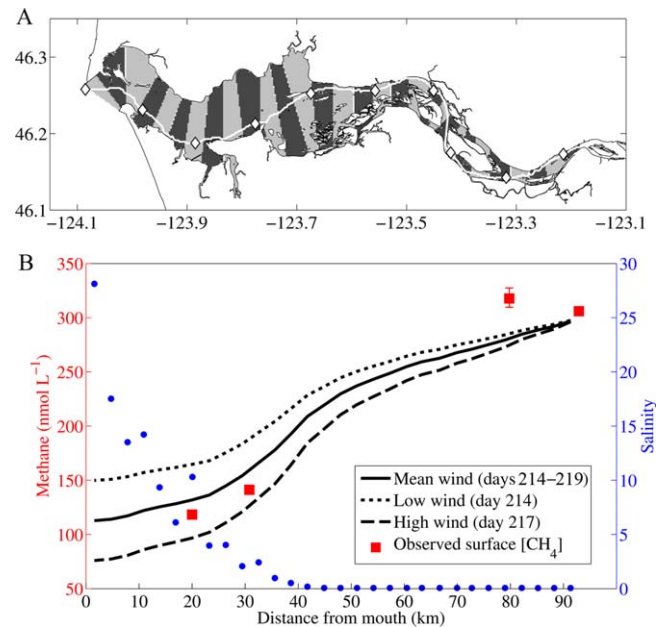


Fig. 9. (A) Polygons with 3 km along-channel width used to estimate along-estuary atmospheric fluxes. The white line traces the deepest point of the main channel with diamonds at 10 km intervals. (B) Along-channel methane gradient predicted from Eq. 8 with an initial concentration of 300 nmol m^{-3} at river 93 km and with three wind cases. Red squares are methane concentration (mean \pm s.d.) in surface water samples collected on days 216 and 217. Blue circles are the mean near-surface salinity measured by the ship's flow-through system within each polygon. [Color figure can be viewed in the online issue, which is available at wileyonlinelibrary.com.]

A limited number of methane concentration data were available for comparison to the predicted gradient. Methane samples were collected at three stations downstream of BAT (red markers in Fig. 9B). Unlike the predicted gradient, the observed concentration did not decrease in the first 13 km. The higher observed methane concentration could have been caused by lateral inputs of methane in that stretch of the river, variability in the history of riverine methane input, unresolved cross-channel gradients (Anthony et al. 2012), or a cumulative effect of gas exchange variability. Further downstream (river km 20–30), the observed surface methane concentrations fell between the methane loss model prediction for the average and upper range of daily wind speeds near the time of the survey (Fig. 9B).

Discussion

Plume transport observations

Measuring fluxes through the estuary–ocean boundary is a significant challenge in the development of estuarine biogeochemical budgets. A methodological advancement in sampling biogeochemical transports in physically complex regions was achieved in this study by coupling three advanced instrumentation techniques (SuperSucker, FMA

with membrane contactor, and ADCP). This system was successfully deployed in a region of strong tidal variability at the mouth of the CRE to produce detailed observations of methane transport between the estuary and coastal ocean (Figs. 5-7; Table 1). Before discussing the application to the Columbia River methane budget as a whole, we examine challenges and benefits of obtaining estuary-ocean methane transports from the SuperSucker.

The placement of the survey line in the near-field plume and the ~ 3 h duration of each transect introduced uncertainty in the tidally averaged transports. The near-field plume is an inertial jet during ebb conditions but not during flood conditions (Horner-Devine et al. 2009; Kilcher et al. 2012). Due to this typical pattern of ebb-flood asymmetry in tidal exchange at the estuary mouth (Stommel and Farmer 1952; Chadwick and Largier 1999), the plume transects did not fully enclose the return flow. This design provided a bias toward offshore transport as can be seen in section-integrated volume transport over the tide cycle (Fig. 7A), with maximum shoreward transport only 20% of the maximum volume transport away from shore. Additional offshore transport bias may arise from near-field plume circulation (Horner-Devine et al. 2009) and ambient along-shelf flow. In the latter case, our correction for shoreward flow could be overestimated by as much as $3 \times 10^3 \text{ m}^3 \text{ s}^{-1}$ given summertime observations of 0.03 m s^{-1} southward flow along the coast (Kirincich and Barth 2009). The importance of sampling a closed section is highlighted by these sources of uncertainty in the transport estimates that arise from the highly spatially variable dynamics in the near-field plume region.

The sampling challenge highlighted here is not unique to the mouth of the Columbia River, but common to many moderate-large river systems. In fact, the use of the SuperSucker greatly improved our ability to adequately sample methane export from the CRE mouth compared to the traditional method of collecting discrete water samples. The difference is exemplified in the variability in freshwater end-members obtained from extrapolation of methane-salinity relationships, as in Fig. 6. Multiplied by river discharge at the time of the survey, the apparent freshwater end-members from individual transects would produce estimated transports out of the estuary of $2.6\text{--}5.2 \times 10^4 \text{ mol d}^{-1}$, a range larger than the uncertainty in the tidally averaged SuperSucker transects (Table 1). Although not a focus of this article, the SuperSucker survey also provided spatial and temporal details of methane dynamics in the near-field plume, such as the images displayed in Fig. 5, which would be impossible to obtain by traditional sampling methods. High-resolution biogeochemical concentration data reduce the chance of sampling bias for biogeochemical fluxes in regions with complex physical dynamics.

CRE methane budget

A major motivation for measuring methane transport in the Columbia River was to assess whether lateral supply of

methane in the lower river and estuary significantly impacts methane export from the system. Our results indicate that quantitatively significant lateral sources of methane were not required to balance the methane budget for the lower Columbia River in early August 2010 (Table 1). In the base case of river discharge and wind speed averaged over a 6-d period, the estimated input of methane due to transport through the river boundary was balanced within 5% by losses due to transport through the ocean boundary, air-sea exchange, and microbial oxidation. The budget had a deficit of $6.3 \times 10^3 \text{ mol d}^{-1}$ in the loss terms. Because observed methane concentrations fell between the average and high wind speed cases (Fig. 9B), it is also reasonable to consider the higher wind case, which required $7.8 \times 10^3 \text{ mol d}^{-1}$ additional supply within the control volume, or $\sim 6\%$ of the total methane inputs.

Estimated errors in the methane budget leave room for additional methane supply or loss within the control volume on the order of 25% of the budget. The uncertainty bounds presented in Table 1 were estimated from minimum and maximum daily winds and river discharge within a week of the plume survey, and from variations in the method of calculating transport in the plume. A combination of lower river discharge, higher wind, and higher plume transport (derived from imposing 40% lower methane concentration in high salinity water for the landward flow correction) requires an additional supply of methane of $31.2 \times 10^3 \text{ mol d}^{-1}$. A combination of higher river discharge, lower wind speeds, and lower plume transport (due to temporal aliasing correction) requires additional methane losses of $41.3 \times 10^3 \text{ mol d}^{-1}$ (Table 1).

One source of uncertainty not quantified in Table 1 was the spatial and temporal variability of methane near the river boundary. The river end-member concentration served as both the initial condition for the methane loss model and the basis of the river methane transport term. River methane concentration data in this study were only available from a single profile at the start of the survey, although observations from other years and variability observed further upstream in the watershed (see "Methane transport in river") suggest that methane loading is not widely variable, especially on the week-long time scale relevant to our budget calculations. More generally, the maintenance of methane supersaturation in the river source waters involves net production in the balances of subsurface methanogenesis and methane oxidation (Kelley et al. 1995; Deborde et al. 2010; Shelley et al. 2015) and persistent exchange of water from the subsurface to the surface (Chanton et al. 1989; Jones and Mulholland 1998; Borges and Abril 2012). Understanding these pathways is important for constraining downstream methane budgets, such as the one constructed in our study, and connections with other biogeochemical cycles involving sediment-water fluxes (Charette and Sholkovitz 2006; Cook et al. 2007; Kim et al. 2012).

Table 2. Comparison of CRE methane budget with methane budgets in other systems. Duration of the studies varied, as listed in footnotes. Estimates of lateral supply include direct measurement of fluxes from sediments and tidal creeks and/or budget closure terms.

Estuary	River discharge ($\text{m}^3 \text{s}^{-1}$)	River methane (nmol L^{-1})	Lateral supply (% of total)	Air-sea flux ($\text{mol m}^{-2} \text{d}^{-1}$)	% to atmosphere	% to ocean
Columbia River,* August	4500	300	<10	1×10^{-4}	42	32
Changjiang River [†]	28,000	80	25	0.7×10^{-4}	>100 [†]	0
lower Lena River [‡]	22,600	70	90	1×10^{-2}	80	20
Buor Khaya Bay [‡]	22,600	115	0	6×10^{-5}	100	0
Hudson River, [§] March	850	235	88	6×10^{-4}	64	36
Hudson River, [§] August	150	235	96	6×10^{-4}	50	3
Arcachon Lagoon [¶]	30	460	53	0.5×10^{-4}	100	0

*This study (August 2010).

[†]Zhang et al. (2008), annual budget. Estimated flux to atmosphere exceeded observed methane sources.

[‡]Bussman (2013), results for summertime data from freshwater Lena River delta with creeks draining permafrost and for the brackish Buor Khaya Bay fed by Lena River delta.

[§]De Angelis and Scranton (1993), results from 3-d long surveys in March and August 1991.

[¶]Deborde et al. (2010), annual budget.

Spatial and temporal variability in rates of aerobic microbial oxidation of methane in water column is another topic needing further study. The methane loss model used mean oxidation rates in fresh water from a single survey of the Columbia (Lilley et al. 1996), adjusted for seasonal temperature change. Summertime methane oxidation rates observed in a study of the Hudson River were nearly a factor of 10 higher (De Angelis and Scranton 1993). At these higher oxidation rates the predicted methane loss in the lower Columbia would be 47% higher and thus require significant supply of methane within the estuary. However, the rates observed in the Hudson River are likely not applicable to the Columbia due to a large difference in turbidity levels in the two systems (5–20 mg L^{-1} in Columbia (Sullivan et al. 2001), 100–5000 mg L^{-1} in Hudson (Geyer et al. 2001)) and an association between methane oxidizing bacteria and suspended particles (Sanson and Martens 1978; De Angelis and Scranton 1993; Abril et al. 2007).

Estuaries and larger rivers are in a transition zone between air-sea gas exchange dominated by wind-driven turbulence as in the open ocean (Wanninkhof 1992; Ho et al. 2006) or by river flow characteristics as in shallower streams and rivers (Raymond et al. 2012). An alternative parameterization derived from natural and purposeful tracers in estuaries and rivers (Raymond and Cole 2001) does not deviate much from Eq. 9 at the relatively low wind speeds experienced in this study. Furthermore, water depths in the lower Columbia River are sufficient to justify a wind-based gas exchange parameterization, as in the Hudson River estuary (Clark et al. 1994; Ho et al. 2011) and larger portions of the Amazon river system (Alin et al. 2011). However, considerable spatial variability in methane outgassing has been observed further upstream in the Columbia River (Lilley et al. 1996) and locations of enhanced turbulence are apparent in boils visible at

the surface in the lower river and estuary (personal observation). Further uncertainty arises from the application of wind speed measured at a single location; spatial variability in wind speed along the river may be large (e.g., Sharp and Mass 2004). A small number of observations of surface methane concentration at the time of the survey fell between the average and high wind cases in the methane loss model (Fig. 9). The model-data comparison suggests that either (1) the higher winds are a better representation of what the surface waters were exposed to, (2) the wind-based gas exchange parameterization is an underestimate of exchange rate, or (3) oxidation rates used in the model were too low.

Methane cycling in estuaries

Detailed methane budgets have been constructed for a handful of other river and estuarine systems, including a shallow lagoon (Deborde et al. 2010), drainage from high latitude permafrost areas (Bussmann 2013), and estuaries with moderate (Hudson River; De Angelis and Scranton 1993) and large (Changjiang River; Zhang et al. 2008) freshwater input. None of these prior studies, however, directly measured methane transport through the estuary-ocean boundary. Despite differences in how each methane budget was developed, these studies provide comparisons of methane pathways and partitioning in a range of estuary types. Table 2 summarizes the methane cycling characteristics of these other systems compared with our results for the CRE.

In contrast to our observation that one third of the riverine methane supply was transported through the mouth of the CRE, most of these studies found little to no export of methane to the coastal ocean (De Angelis and Scranton 1993; Zhang et al. 2008; Deborde et al. 2010). One exception was an observation of 36% of the methane supply reaching the estuary mouth in the Hudson River at a time of year

when cold water temperatures suppressed microbial oxidation of methane and estuary residence time was likely shorter (De Angelis and Scranton 1993). The proportion of riverine methane exported to the ocean should depend on rates of methane losses within the estuary relative to flushing times, so it follows that the rapidly flushed CRE had a relatively large loss to the ocean.

Another contrast between the CRE results and previously constructed methane budgets is in the importance of lateral or benthic supply of methane within the estuary. Excess methane was noted in mesohaline water in several European estuaries, although the contribution of those sources to the total methane budget was not calculated (Middelburg et al. 2002). Fluxes of methane from the sediments contributed at least 25% of the methane supply in estuaries ranging from the shallow Arcachon Lagoon (Deborde et al. 2010) to the river-dominated Changjiang Estuary (Zhang et al. 2008). In the Lena River Delta and lower Hudson River, supply of methane from lateral sources exceeded the riverine supply (De Angelis and Scranton 1993; Bussmann 2013). Measurements of methane fluxes at the sediment–water interface are needed in the CRE to better understand the lateral sources of methane and to test the inference from our system-wide budgeting approach that such lateral supply is minor compared with delivery from the river.

Our CRE methane budget confirms high air–sea fluxes of methane on a per area basis found by other studies (Table 2). Given the small footprint of estuaries and rivers, however, this study also confirms that contributions of methane to the global budget are likely small (De Angelis and Lilley 1987; Middelburg et al. 2002; Borges and Abril 2012). Another important consideration is the degree to which the flux of methane to the atmosphere is reduced by oxidation in the water column. Our budget estimates that close to a quarter of the riverine methane supply is consumed by methanotrophic bacteria within the estuary. Stable isotopic ratios from a previous study of the lower CRE support the conclusion that the methane pool is impacted by microbial oxidation (Sansone et al. 1999). Rates of methane oxidation in estuaries can be much higher than assumed in our model, such as summertime rates observed in the Hudson River that reduced methane supply by half (De Angelis and Scranton 1993) or significantly elevated oxidation rates in an estuary turbidity maximum of the Gironde Estuary (Abril et al. 2007). Methanotrophic activity varies with factors including temperature, salinity, and suspended particle load (De Angelis and Scranton 1993; Hanson and Hanson 1996). Future change in environmental conditions, such as an increase in mean water temperature, has the potential to greatly alter methane cycling in estuaries by changing the balance of loss by microbial oxidation and flux to the atmosphere.

Patterns of methane injection are relevant to those expected for other reduced substrates produced under suboxic to anoxic conditions as a consequence of organic matter

rem mineralization in permeable subsurface settings, such as ammonium and phosphate (Whiting and Childers 1989; Jahnke et al. 2003; Deborde et al. 2008) and trace elements (Sunda and Kieber 1994; Charette and Sholkovitz 2006). Unlike methane, these other metabolic products have the potential to significantly impact primary productivity and other major carbon cycling functions in estuaries. Supply of these more bioreactive chemicals via groundwater or hyporheic exchange is likely ubiquitous but often overlooked in estuary nutrient budgets (Valiela et al. 1990; Liefer et al. 2013; Makings et al. 2014). As a constituent with relatively simple cycling in the water column, well-established estuarine budgets of methane can help constrain the significance of lateral inputs of other products of organic matter metabolism.

References

- Abril, G., M. Commarieu, and F. Guérin. 2007. Enhanced methane oxidation in an estuarine turbidity maximum. *Limnol. Oceanogr.* **52**: 470–475. doi:10.4319/lo.2007.52.1.0470
- Alin, S. R., M.D.F.F.L. Rasera, C. I. Salimon, J. E. Richey, G. W. Holtgrieve, A. V. Krusche, and A. Snidvongs. 2011. Physical controls on carbon dioxide transfer velocity and flux in low-gradient river systems and implications for regional carbon budgets. *J. Geophys. Res. Biogeosci.* **116**: G01009. doi:10.1029/2010JG001398
- Anthony, S. E., F. G. Prahl, and T. D. Peterson. 2012. Methane dynamics in the Willamette River, Oregon. *Limnol. Oceanogr.* **57**: 1517–1530. doi:10.4319/lo.2012.57.5.1517
- Bandstra, L., B. Hales, and T. Takahashi. 2006. High-frequency measurements of total CO₂: Method development and first oceanographic observations. *Mar. Chem.* **100**: 24–38. doi:10.1016/j.marchem.2005.10.009
- Bange, H., U. Bartell, S. Rapsomanikis, and M. Andreae. 1994. Methane in the Baltic and North Seas and a reassessment of the marine emissions of methane. *Global Biogeochem. Cycles.* **8**: 465–480, doi: 10.1029/94GB02181
- Baptista, A., Y. Zhang, and A. Chawla. 2005. A cross-scale model for 3D baroclinic circulation in estuary–plume–shelf systems: II. Application to the Columbia River. *Cont. Shelf Res.* **25**: 935–972. doi:10.1016/j.csr.2004.12.003
- Barnes, C. A., A. C. Duxbury, and B. Morse. 1972. Circulation and selected properties of the Columbia River effluent at sea, p. 41–80. *In* A. Pruter and D. Alverson [eds.], *The Columbia River estuary and adjacent ocean waters*. Univ. of Washington Press.
- Borges, A., and G. Abril. 2012. Carbon dioxide and methane dynamics in estuaries, p. 119–161. *In* E. Wolanski and D. McLusky [eds.], *Treatise on estuarine and coastal science volume 5: Biogeochemistry*. Academic Press.
- Bugna, G. C., J. P. Chanton, J. E. Cable, W. C. Burnett, and P. H. Cable. 1996. The importance of groundwater

- discharge to the methane budgets of nearshore and continental shelf waters of the northeastern Gulf of Mexico. *Geochim. Cosmochim. Acta.* **60**: 4735–4746. doi:10.1016/S0016-7037(96)00290-6
- Bussmann, I. 2013. Distribution of methane in the Lena Delta and Buor-Khaya Bay, Russia. *Biogeosciences* **10**: 4641–4652. doi:10.5194/bg-10-4641-2013
- Carignan, K. S., L. A. Taylor, B. W. Eakins, and R. R. Warnken. 2009. Digital elevation model of Astoria, Oregon: Procedures, data sources and analysis. NOAA Technical Memorandum NESDIS NGDC-22.
- Chadwick, D., and J. Largier. 1999. Tidal exchange at the bay-ocean boundary. *J. Geophys. Res.* **104**: 29901–29924. doi:10.1029/1999JC900165
- Chanton, J. P., C. S. Martens, and C. A. Kelley. 1989. Gas transport from methane-saturated, tidal freshwater and wetland sediments. *Limnol. Oceanogr.* **34**: 807–819. doi:10.4319/lo.1989.34.5.0807
- Charette, M. A., and E. R. Sholkovitz. 2006. Trace element cycling in a subterranean estuary: Part 2. Geochemistry of the pore water. *Geochim. Cosmochim. Acta.* **70**: 811–826. doi:10.1016/j.gca.2005.10.019
- Clark, J., R. Wanninkhof, P. Schlosser, and H. Simpson. 1994. Gas exchange rates in the tidal Hudson River using a dual tracer technique. *Tellus B.* **46B**: 274–285. doi:10.1034/j.1600-0889.1994.t01-2-00003.x
- Cook, P. L. M., F. Wenzhöfer, R. N. Glud, F. Janssen, and M. Huettel. 2007. Benthic solute exchange and carbon mineralization in two shallow subtidal sandy sediments: Effect of advective pore-water exchange. *Limnol. Oceanogr.* **52**: 1943–1963. doi:10.4319/lo.2007.52.5.1943
- Cudaback, C., and D. Jay. 2000. Tidal asymmetry in an estuarine pycnocline: Depth and thickness. *J. Geophys. Res.* **105**: 26237–26251. doi:10.1029/2000JC900135
- De Angelis, M., and M. Lilley. 1987. Methane in surface waters of Oregon estuaries and rivers. *Limnol. Oceanogr.* **32**: 716–722. doi:10.4319/lo.1987.32.3.0716
- De Angelis, M., and M. Scranton. 1993. Fate of methane in the Hudson River and estuary. *Global Biogeochem. Cycles.* **7**: 509–523. doi:10.1029/93GB01636
- Deborde, J., and others. 2008. Role of tidal pumping on nutrient cycling in a temperate lagoon (Arcachon Bay, France). *Mar. Chem.* **109**: 98–114. doi:10.1016/j.marchem.2007.12.007
- Deborde, J., and others. 2010. Methane sources, sinks and fluxes in a temperate tidal Lagoon: The Arcachon lagoon (SW France). *Estuar. Coast. Shelf Sci.* **89**: 256–266. doi:10.1016/j.ecss.2010.07.013
- Geyer, W. R., J. D. Woodruff, and P. Traykovski. 2001. Sediment transport and trapping in the Hudson River estuary. *Estuaries* **24**: 670. doi:10.2307/1352875
- Gonzalez-Valencia, R., and others. 2014. In situ measurement of dissolved methane and carbon dioxide in freshwater ecosystems by off-axis integrated cavity output spectroscopy. *Environ. Sci. Technol.* **48**: 11421–11428. doi:10.1021/es500987j
- Grunwald, M., and others. 2009. Methane in the southern North Sea: Sources, spatial distribution and budgets. *Estuar. Coast. Shelf Sci.* **81**: 445–456. doi:10.1016/j.ecss.2008.11.021
- Hales, B., and T. Takahashi. 2002. The pumping SeaSoar: A high-resolution seawater sampling platform. *J. Atmos. Ocean. Technol.* **19**: 1096–1104. doi:10.1175/1520-0426(2002)019<1096:TPSAHR>2.0.CO;2
- Hales, B., and T. Takahashi. 2004. High-resolution biogeochemical investigation of the Ross Sea, Antarctica, during the AESOPS (U. S. JGOFS) Program. *Global Biogeochem. Cycles.* **18**: GB3006. doi:10.1029/2003GB002165
- Hales, B., D. Chipman, and T. Takahashi. 2004. High-frequency measurement of partial pressure and total concentration of carbon dioxide in seawater using microporous hydrophobic membrane contactors. *Limnol. Oceanogr. Methods.* **2**: 356–364. doi:10.4319/lom.2004.2.356
- Hales, B., J. N. Moum, P. Covert, and A. Perlin. 2005. Irreversible nitrate fluxes due to turbulent mixing in a coastal upwelling system. *J. Geophys. Res.* **110**: C10S11. doi:10.1029/2004JC002685
- Hales, B., L. Karp-Boss, A. Perlin, and P. A. Wheeler. 2006. Oxygen production and carbon sequestration in an upwelling coastal margin. *Global Biogeochem. Cycles.* **20**: GB3001. doi:10.1029/2005GB002517
- Hales, B., and T. Takahashi. 2012. Mesoscale biogeochemical responses to iron fertilization in the upper layers of the Southern Ocean Iron Experiment areas. *J. Geophys. Res.* **117**: C01018. doi:10.1029/2011JC006956
- Hanson, R. S., and T. E. Hanson. 1996. Methanotrophic bacteria. *Microbiol. Rev.* **60**: 439–471.
- Hickey, B., L. Pietrafesa, D. Jay, and W. Boicourt. 1998. The Columbia River plume study: Subtidal variability in the velocity and salinity fields. *J. Geophys. Res.* **103**: 10339–10368. doi:10.1029/97JC03290
- Ho, D. T., C. S. Law, M. J. Smith, P. Schlosser, M. Harvey, and P. Hill. 2006. Measurements of air-sea gas exchange at high wind speeds in the Southern Ocean: Implications for global parameterizations. *Geophys. Res. Lett.* **33**: L16611. doi:10.1029/2006GL026817
- Ho, D. T., P. Schlosser, and P. M. Orton. 2011. On factors controlling air–water gas exchange in a large tidal river. *Estuar. Coast.* **34**: 1103–1116. doi:10.1007/s12237-011-9396-4
- Holser, R. R., M. A. Goni, and B. Hales. 2011. Design and application of a semi-automated filtration system to study the distribution of particulate organic carbon in the water column of a coastal upwelling system. *Mar. Chem.* **123**: 67–77. doi:10.1016/j.marchem.2010.10.001
- Horner-Devine, A. R. 2009. The bulge circulation in the Columbia River plume. *Cont. Shelf Res.* **29**: 234–251. doi:10.1016/j.csr.2007.12.012

- Horner-Devine, A. R., D. A. Jay, P. M. Orton, and E. Y. Spahn. 2009. A conceptual model of the strongly tidal Columbia River plume. *J. Mar. Syst.* **78**: 460–475. doi:10.1016/j.jmarsys.2008.11.025
- Jahnke, R. A., C. R. Alexander, and J. E. Kostka. 2003. Advective pore water input of nutrients to the Satilla River Estuary, Georgia, USA. *Estuar. Coast. Shelf Sci.* **56**: 641–653. doi:10.1016/S0272-7714(02)00216-0
- Jay, D. A., and J. D. Smith. 1990. Circulation, density distribution and neap-spring transitions in the Columbia River Estuary. *Prog. Oceanogr.* **25**: 81–112. doi:10.1016/0079-6611(90)90004-L
- Jones, J., and P. Mulholland. 1998. Methane input and evasion in a hardwood forest stream: Effects of subsurface flow from shallow and deep pathways. *Limnol. Oceanogr.* **43**: 1243–1250. doi:10.4319/lo.1998.43.6.1243
- Kärnä, T., A. M. Baptista, J. E. Lopez, P. J. Turner, C. McNeil, and T. B. Sanford. 2015. Numerical modeling of circulation in high-energy estuaries: A Columbia River estuary benchmark. *Ocean Model.* **88**: 54–71. doi:10.1016/j.ocemod.2015.01.001
- Kelley, C., C. Martens, and W. Ussler. 1995. Methane dynamics across a tidally flooded riverbank margin. *Limnol. Oceanogr.* **40**: 1112–1129. doi:10.4319/lo.1995.40.6.1112
- Kilcher, L. F., and J. D. Nash. 2010. Structure and dynamics of the Columbia River tidal plume front. *J. Geophys. Res.* **115**: C05S90. doi:10.1029/2009JC006066
- Kilcher, L. F., J. D. Nash, and J. N. Moum. 2012. The role of turbulence stress divergence in decelerating a river plume. *J. Geophys. Res.* **117**: C05032. doi:10.1029/2011JC007398
- Kim, T. H., H. Waska, E. Kwon, I. G. N. Suryaputra, and G. Kim. 2012. Production, degradation, and flux of dissolved organic matter in the subterranean estuary of a large tidal flat. *Mar. Chem.* **142–144**: 1–10. doi:10.1016/j.marchem.2012.08.002
- Kirincich, A. R., and J. A. Barth. 2009. Alongshelf variability of inner-shelf circulation along the central Oregon coast during summer. *J. Phys. Oceanogr.* **39**: 1380–1398. doi:10.1175/2008JPO3760.1
- Le Mer, J., and P. Roger. 2001. Production, oxidation, emission and consumption of methane by soils: A review. *Eur. J. Soil Biol.* **37**: 25–50. doi:10.1016/S1164-5563(01)01067-6
- Liefer, J. D., H. L. MacIntyre, N. Su, and W. C. Burnett. 2013. Seasonal alternation between groundwater discharge and benthic coupling as nutrient sources in a shallow coastal lagoon. *Estuar. Coast.* **37**: 925–940. doi:10.1007/s12237-013-9739-4
- Lilley, M., M. de Angelis, and E. Olson. 1996. Methane concentrations and estimated fluxes from Pacific Northwest rivers. *Mitteilungen Int. Vereinigung für Theor. und Angew. Limnol.* **25**: 187–196.
- MacCready, P. 2011. Calculating estuarine exchange flow using isohaline coordinates. *J. Phys. Oceanogr.* **41**: 1116–1124. doi:10.1175/2011JPO4517.1
- Makings, U., I. R. Santos, D. T. Maher, L. Golsby-Smith, and B. D. Eyre. 2014. Importance of budgets for estimating the input of groundwater-derived nutrients to an eutrophic tidal river and estuary. *Estuar. Coast. Shelf Sci.* **143**: 65–76. doi:10.1016/j.ecss.2014.02.003
- McCabe, R. M., B. M. Hickey, and P. MacCready. 2008. Observational estimates of entrainment and vertical salt flux in the interior of a spreading river plume. *J. Geophys. Res.* **113**: C08027. doi:10.1029/2007JC004361
- Megonigal, J., and S. Neubauer. 2009. Biogeochemistry of tidal freshwater wetlands, p. 535–562. *In* G. M. E. Perillo, E. Wolanski, D. R. Cahoon, and M. M. Brinson [eds.], *Coastal Wetlands: An integrated ecosystem approach*. Elsevier.
- Middelburg, J., J. Nieuwenhuize, and N. Iversen. 2002. Methane distribution in European tidal estuaries. *Biogeochemistry* **59**: 95–119. doi:10.1023/A:1015515130419
- Nash, J. D., L. F. Kilcher, and J. N. Moum. 2009. Structure and composition of a strongly stratified, tidally pulsed river plume. *J. Geophys. Res.* **114**: C00B12. doi:10.1029/2008JC005036
- Neal, V. 1972. Physical aspects of the Columbia River and its estuary, p. 19–39. *In* A. Pruter and D. Alverson [eds.], *The Columbia River estuary and adjacent ocean waters*. Univ. of Washington Press.
- Orton, P. M., and D. A. Jay. 2005. Observations at the tidal plume front of a high-volume river outflow. *Geophys. Res. Lett.* **32**: L11605. doi:10.1029/2005GL022372
- Raymond, P. A., and J. J. Cole. 2001. Gas exchange in rivers and estuaries : Choosing a gas transfer velocity. *Estuaries* **24**: 312–317. doi:10.2307/1352954
- Raymond, P. A., and others. 2012. Scaling the gas transfer velocity and hydraulic geometry in streams and small rivers. *Limnol. Oceanogr. Fluids Environ.* **2**: 41–53. doi:10.1215/21573689-1597669
- RDI. 2011. Acoustic Doppler current profiler: Principles of operation, a practical primer. P/N 951-6069-00. Teledyne RD Instruments, Poway, California.
- Reeburgh, W. S. 2007. Oceanic methane biogeochemistry. *Chem. Rev.* **107**: 486–513. doi:10.1021/cr050362v
- Sanson, F. J., and C. S. Martens. 1978. Methane oxidation in Cape Lookout Bight, North Carolina. *Limnol. Oceanogr.* **23**: 349–355. doi:10.4319/lo.1978.23.2.0349
- Sansone, F. J., M. E. Holmes, and B. N. Popp. 1999. Methane stable isotopic ratios and concentrations as indicators of methane dynamics in estuaries watershed of the river mouth. *Global Biogeochem. Cycles* **13**: 463–474. doi:10.1029/1999GB900012
- Sharp, J., and C. F. Mass. 2004. Columbia gorge gap winds: Their climatological influence and synoptic evolution. *Weather Forecast.* **19**: 970–992. doi:10.1175/826.1
- Shelley, F., F. Abdullahi, J. Grey, and M. Trimmer. 2015. Microbial methane cycling in the bed of a chalk river: Oxidation has the potential to match methanogenesis

- enhanced by warming. *Freshw. Biol.* **60**: 150–160. doi:[10.1111/fwb.12480](https://doi.org/10.1111/fwb.12480)
- Sherwood, C., and J. Creager. 1990. Sedimentary geology of the Columbia River estuary. *Prog. Oceanogr.* **25**: 15–79. doi:[10.1016/0079-6611\(90\)90003-K](https://doi.org/10.1016/0079-6611(90)90003-K)
- Simenstad, C. A., L. F. Small, C. D. McIntire, D. A. Jay, and C. Sherwood. 1990. Columbia River estuary studies: An introduction to the estuary, a brief history, and prior studies. *Prog. Oceanogr.* **25**: 1–13. doi:[10.1016/0079-6611\(90\)90002-J](https://doi.org/10.1016/0079-6611(90)90002-J)
- Stommel, H., and H. G. Farmer. 1952. On the nature of estuarine circulation part I. Ref. 52–88. Woods Hole Oceanographic Institution.
- Sullivan, B., F. Prahl, L. Small, and P. Covert. 2001. Seasonality of phytoplankton production in the Columbia River: A natural or anthropogenic pattern? *Geochim. Cosmochim. Acta.* **65**: 1125–1139. doi:[10.1016/S0016-7037\(00\)00565-2](https://doi.org/10.1016/S0016-7037(00)00565-2)
- Sunda, W. G., and D. J. Kieber. 1994. Oxidation of humic substances by manganese oxides yields low-molecular-weight organic substrates. *Nature* **367**: 62–64. doi:[10.1038/367062a0](https://doi.org/10.1038/367062a0)
- Upstill-Goddard, R. C., J. Barnes, T. Frost, S. Punshon, and N. J. P. Owens. 2000. Methane in the southern North Sea: Low-salinity inputs, estuarine removal, and atmospheric flux. *Global Biogeochem. Cycles* **14**: 1205. doi:[10.1029/1999GB001236](https://doi.org/10.1029/1999GB001236)
- Valiela, I., J. Costa, K. Foreman, J. M. Teal, B. Howes, and D. Aubrey. 1990. Transport of groundwater-borne nutrients from watersheds and their effects on coastal waters. *Biogeochemistry* **10**: 177–197. doi:[10.1007/BF00003143](https://doi.org/10.1007/BF00003143)
- Wanninkhof, R. 1992. Relationship between wind speed and gas exchange. *J. Geophys. Res.* **97**: 7373–7382. doi:[10.1029/92JC00188](https://doi.org/10.1029/92JC00188)
- Wanninkhof, R. 2014. Relationship between wind speed and gas exchange over the ocean revisited. *Limnol. Oceanogr.: Methods.* **12**: 351–362. doi:[10.4319/lom.2014.12.351](https://doi.org/10.4319/lom.2014.12.351)
- Ward, B. B., K. A. Kilpatrick, P. C. Novelli, and M. I. Scranton. 1987. Methane oxidation and methane fluxes in the ocean surface layer and deep anoxic waters. *Nat. Lett.* **327**: 226–229. doi:[10.1038/327226a0](https://doi.org/10.1038/327226a0)
- Ward, B. B., K. A. Kilpatrick, A. E. Wopat, E. C. Minnich, and M. E. Lidstrom. 1989. Methane oxidation in Saanich Inlet during summer stratification. *Cont. Shelf Res.* **9**: 65–75. doi:[10.1016/0278-4343\(89\)90083-6](https://doi.org/10.1016/0278-4343(89)90083-6)
- Whiting, G. J., and D. L. Childers. 1989. Subtidal advective water flux as a potentially important nutrient input to southeastern U.S.A. saltmarsh estuaries. *Estuar. Coast. Shelf Sci.* **28**: 417–431. doi:[10.1016/0272-7714\(89\)90089-9](https://doi.org/10.1016/0272-7714(89)90089-9)
- Wiesenburg, D. A., and N. L. Guinasso. 1979. Equilibrium solubilities of methane, carbon monoxide, and hydrogen in water and sea water. *J. Chem. Eng. Data* **24**: 356–360. doi:[10.1021/je60083a006](https://doi.org/10.1021/je60083a006)
- WMO. 2011. The state of greenhouse gases in the atmosphere based on global observations through 2010. WMO Greenh. Gas Bull. **7**: 1–4. ISSN 2078-0796
- Zhang, Y., and A. M. Baptista. 2008. SELFE: A semi-implicit Eulerian–Lagrangian finite-element model for cross-scale ocean circulation. *Ocean Model.* **21**: 71–96. doi:[10.1016/j.ocemod.2007.11.005](https://doi.org/10.1016/j.ocemod.2007.11.005)
- Zhang, G., J. Zhang, S. Liu, J. Ren, J. Xu, and F. Zhang. 2008. Methane in the Changjiang (Yangtze River) estuary and its adjacent marine area: Riverine input, sediment release and atmospheric fluxes. *Biogeochemistry* **91**: 71–84. doi:[10.1007/s10533-008-9259-7](https://doi.org/10.1007/s10533-008-9259-7)

Acknowledgments

This manuscript was prepared in memory of Murray Levine. Field work was made possible by assistance from Margaret Sparrow, Dale Hubbard, and the R/V *Wecoma* captain and crew. We thank Antonio Baptista, Paul Turner, and other members of the CMOP modeling team for providing output from the SELFE model and Charles Seaton for processing bathymetry data. This work was supported by funding from the National Science Foundation of the Science and Technology Center for Coastal Margin Observation and Prediction (CMOP) under cooperative agreement OCE-042460.

Submitted 3 November 2014

Revised 3 July 2015, 24 September 2015

Accepted 29 September 2015

Associate editor: Peter Hernes